Nano Research
2022, 15(9): 8665–8672

ISSN 1998-0124 CN 11-5974/O4
https://doi.org/10.1007/s12274-022-4478-0

Research Article

Direct assembly between closed-shell coinage metal superatoms

Famin Yu[1], Yu Zhu[1], Yang Gao[2], Rui Wang[1], Wanrong Huang[1], Yi Gao[3] (✉), and Zhigang Wang[1] (✉)

[1] *Institute of Atomic and Molecular Physics, Jilin University, Changchun 130012, China*
[2] *Center Énergie Matériaux et Télécommunications, Institut National de la Recherche Scientifique (INRS), Varennes, Québec J3X 1P7k, Canada*
[3] *Shanghai Advanced Research Institute, Chinese Academy of Sciences, Shanghai 201210, China*

Received: 20 February 2022 / **Revised:** 14 April 2022 / **Accepted:** 28 April 2022

ABSTRACT

Bottom-up constructing all-metal functional materials is challenging, because the metal clusters are prone to lose their original structures during coalensence. In this work, we report that closed-shell coinage metal superatoms can achieve direct chemical bonding without losing their electronic properties. The reason is that the supermolecule formed by two superatoms has the same number of bonding and anti-bonding supermolecular orbitals, in which the bonding orbitals contribute to bonding and the anti-bonding orbitals with anti-phase orbitals delocalized over each monomer to maintain the individual geometric and electronic structural properties. Further analysis indicates the interactions between two superatoms are too weak to break the structure of monomers, which is confirmed by the first-principles molecular dynamics simulations. With these superatoms as the basic units, a series of robust one-dimensional and two-dimensional nanostructures are fabricated. Our findings provide a general strategy to take advantage of superatoms in regulating bonding compared to natural atoms, which paves the way for the bottom-up design of materials with collective properties.

KEYWORDS

superatom, assembly, coinage metal cluster, interaction between superatoms

1 Introduction

The coinage metal (CM) clusters are widely used to construct functional materials and devices owing to the unique electronic properties [1–6]. To ensure their structural integrity and assembly, complex ligands are normally needed [7–13], because the pristine CM clusters usually coalescence as bringing together [14–16]. However, the coating ligands will change the electronic structures of pristine metal clusters and block active sites towards applications, i.e., catalysis [17–21]. Therefore, there is an urgent need to directly assemble clusters without ligands to preserve the structure and properties of each cluster, which is the key for the bottom-up fabrication of the functional materials. To achieve this object, CM clusters with extremely high stability and weak interactions with each other should be employed. During the past decades, despite numerous efforts have been devoted [22–27], this task is still challenging, which becomes the major hurdle for the development of functional materials. Surprisingly, as a special cluster with electronic structure similar to atoms, superatoms can exhibit relatively stable valence shell electronic properties [28–33]. Thus, can stable superatoms formed by CMs be direct bonding?

Past research pointed out superatoms can obtain unique properties by adjusting their size, shape, and composition [1, 34], thereby achieving functional applications in many aspects such as single molecule recognition and detection, etc [35–37]. As structural units, whether it is atoms or superatoms, bonding is the basis for forming materials and even devices [38, 39]. At the atomic level, the bonding between atoms is closely dependent on their electronic structure [1, 40, 41], which provides important potential support for realizing the bonding of superatoms. As we all know, atoms with closed-shell electronic shells cannot form chemical bonds in the natural environment. Compared with a noble atom, a coinage metal superatom is composed of atoms and gives rise to collective behavior, with superatomic molecular orbitals delocalizing the entire system and exhibiting atom-like orbital symmetry. Besides, unlike noble gas atoms, coinage metal atoms on the outer shell are highly chemically active, leading to exhibit rich bonding properties [39]. Therefore, the closed-shell superatoms may be ideal units to realize the non-coalesce assembly of the CM systems.

In this work, by using the sixth subgroup metal (including Cr, Mo, and W) to embed inside the first subgroup CM cages (including Cu_{12}, Ag_{12}, and Au_{12}), a series of closed-shell superatoms are constructed, which can achieve direct bonding without breaking framework among the superatoms. Furthermore, using $W@Au_{12}$ as a model, we explain the mechanism of bonding and construct a variety of assembled structures in which electronic structure properties are similar to the monomer. This research provides a reference for constructing materials or devices while maintaining the properties of CM superatoms.

2 Computational methods

The dispersion-corrected density functional theory (DFT-D3) at Perdew–Burke–Ernzerhof (PBE) level was used in this work [42, 43]. The scalar relativistic (SR) has been taken into account through zeroth-order regular approximations (ZORA) [44]. A

Address correspondence to Yi Gao, gaoyi@zjlab.org.cn; Zhigang Wang, wangzg@jlu.edu.cn

triple-ζ with polarization functions (TZP) Slater basis set was employed, with a [1S^2–2p^6] frozen core for Cr and Cu, a [1S^2–3d^{10}] frozen core for Mo and Ag and a [1s^2–4d^{10}] frozen core for W and Au. The nine monomers and nine direct bonded dimers were optimized and analyzed with vibration frequency calculations at the same level to avoid imaginary frequencies. Because of the high demand for computing resources for heavy elements and big systems, the trimer and tetramer were only optimized at the same level. The energy decomposition analysis (EDA) was used to analyze interactions quantitatively [45, 46]. The energy decomposition formula can be expanded as follows

$$\Delta E_{int} = \Delta E_{Pauli} + \Delta E_{orb} + \Delta E_{elstat} + \Delta E_{disp}$$

The Pauli repulsion term E_{Pauli} represents the energy size term for interorbit destabilization; the orbital term E_{orb} represents the term caused by the intermolecular mixing of fragments; E_{elstat} represents the magnitude of the classical electrostatic interaction force of the system; and the dispersion term E_{disp} represents the dispersion correction energy in the weakly interacting system. Above calculations were performed using the Amsterdam Density Functional (ADF) package [47].

For better analyze the electron density and the composition of orbitals of W@Au$_{12}$-W@Au$_{12}$, and the interaction between two W@Au$_{12}$, the single-point energy calculation for W@Au$_{12}$-W@Au$_{12}$ (the structure was obtained by ADF) is performed by Gaussian 09 package [48] using PBE functional as well as the Stuttgart-Dresden (SDD) pseudopotential and basis set. Further, the electron density and the composition of supermolecular orbitals (SMOs), as well as bond critical points (BCPs) and independent gradient model based on Hirshfeld partition of molecular density (IGMH) analyses are performed [49].

Then, in order to study the thermodynamic stability of the assembled structures, the first-principles molecular dynamics simulation (FPMD) was performed for W@Au$_{12}$-W@Au$_{12}$ and W@Cu$_{12}$-W@Cu$_{12}$ [50]. The simulation time was set to 15 ps, and the time step was 1 fs. FPMD implemented constant atomic number N, volume V, and temperature T (NVT) in cp2k [51].

3 Results and discussion

By embedding sixth subgroup metal elements (including Cr, Mo, and W) into the first subgroup CM cages (Cu$_{12}$, Ag$_{12}$, and Au$_{12}$), Cr@Cu$_{12}$ [52], Cr@Ag$_{12}$ [53], Cr@Au$_{12}$ [54], Mo@Cu$_{12}$ [54], Mo@Ag$_{12}$ [53], Mo@Au$_{12}$ [55], W@Cu$_{12}$, W@Ag$_{12}$ [53], and W@Au$_{12}$ [55, 56] can be formed and the structural representation is listed in Fig. 1(a). Their geometric structures all show I_h symmetry. Meanwhile, the six valence electrons of the sixth subgroup elements and the twelve valence electrons of the CM metal cages add up to eighteen valence electrons. Thus, these embedded structures all exhibit the 1S^{2}1P^{6}1D^{10} closed-shell superatomic configuration, which can improve the stability of superatoms [57]. The embedded CM superatoms with high symmetry and high stability shown above may be ideal units for assembly. Among them, the structures of W@Au$_{12}$-W@Au$_{12}$ had already been studied [27], and the most stable bonding mode has been investigated [58]. Based on this, we achieve direct bonding to form nine homodimers, which are W@Au$_{12}$-W@Au$_{12}$, W@Ag$_{12}$-W@Ag$_{12}$, W@Cu$_{12}$-W@Cu$_{12}$, Mo@Au$_{12}$-Mo@Au$_{12}$, Mo@Ag$_{12}$-Mo@Ag$_{12}$, Mo@Cu$_{12}$-Mo@Cu$_{12}$, Cr@Au$_{12}$-Cr@Au$_{12}$, Cr@Ag$_{12}$-Cr@Ag$_{12}$, and Cr@Cu$_{12}$-Cr@Cu$_{12}$, their geometric structures are listed in Table S1 in the Electronic Supplementary Material (ESM).

To investigate whether the M@CM$_{12}$ superatoms can be stable assembled, we first study the interaction between superatoms in dimers using binding energy (E_b), which can be defined as:

$$E_{binding} = \frac{E_1 + E_2 + \cdots + E_n - E_T}{n} \quad (1)$$

where E_1, E_2, …, E_n is the energy of fragments marked from 1 to n, E_T is the total energy, and n is the number of fragments divided. The binding energies of monomers and dimers were shown in

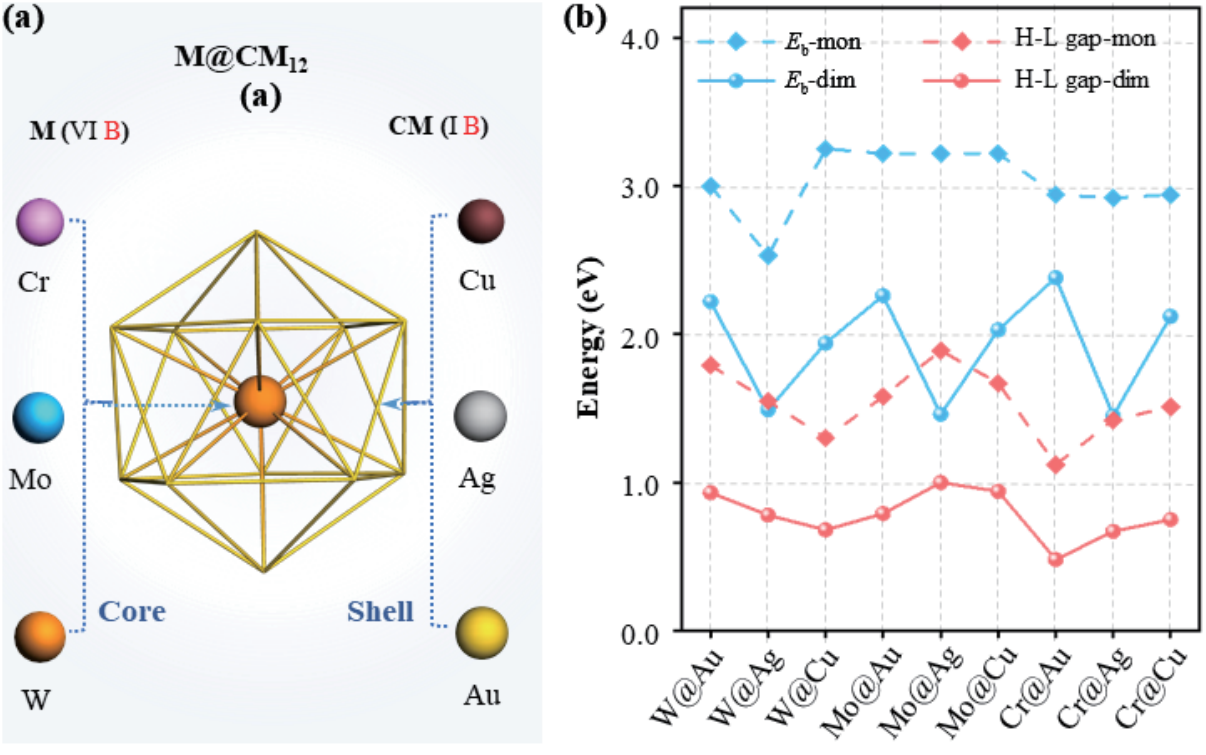

Figure 1 The structural diagram of M@CM$_{12}$ (M = Cr, Mo, and W; CM = Cu, Ag, and Au) and stability analyses of (M@CM$_{12}$)$_2$. (a) "VI B" and "I B" represent the sixth subgroup and the first subgroup. (b) The E_b between superatoms and the HOMO and the LUMO gap of M@CM$_{12}$ and (M@CM$_{12}$)$_2$. The HOMO and LUMO are marked as H and L, and the monomer and dimer are marked as mon and dim.

Fig. 1(b). The results show that the binding energy between two units is between 1.46–2.38 eV, which is smaller than the binding energy per atom (the energy of the superatom relative to the individual atoms) of 2.53–3.25 eV, indicating the interaction between two superatoms is too weak to destroy the original structures [38], ensuring the stability of the assembled dimers.

To discuss the relative weak interactions between two superatoms, we performed the BCPs and independent gradient model based on IGMH analysis by using "atom in molecules" method [59–61]. First, the BCPs data can quantitatively judge the strength of interactions. The result shows the electronic density of BCPs in chemical bonds and center of atoms between two superatoms are smaller than that of bonds between these Au and W atoms (see Fig. S1 and Table S2 in the ESM), indicating the interaction between two superatoms can not break the structure of monomers. In addition, IGMH analysis is a powerful method in analyzing interaction regions between fragments. In this calculation, each $W@Au_{12}$ was defined as an individual fragment, and a thin and broad isosurface appears between two $W@Au_{12}$. The subsurface of interfragment interaction function (δg^{inter}) defined by IGMH clearly exhibits the weak interaction between the two monomers (Fig. S1 in the ESM).

The analysis of binding energy (Fig. 1(b)) also reflects the size of interaction between CM superatoms can be arranged as: Au > Cu > Ag, indicating the weakest interaction between Ag superatoms. Thus, $M@Ag_{12}$ (M = Cr, Mo, and W) may be ideal building blocks. In addition, comparing the highest occupied molecular orbital (HOMO)-the lowest unoccupied molecular orbital (LUMO) gaps of all types of monomers and dimers (Fig. 1(b)), it can be found that the HOMO-LUMO gaps of nine dimers reduce 43%–53%. This little difference of only 10% is caused by the similar properties of nine units formed by the same group. This also indicates that the dimers have higher chemical reactivity than monomers.

To verify the structural stability of dimers, the FPMD was performed for $W@Au_{12}$-$W@Au_{12}$ at 300 K (see Fig. S2 in the ESM). The results show that the dimer structures are well maintained, small structure distortion at each monomer. Moreover, the structural sampling indicated $W@Au_{12}$-$W@Au_{12}$ is among the lowest-energy structures of $W@Au_{12}$ dimers. The HOMO-LUMO gap of $W@Au_{12}$-$W@Au_{12}$ is nearly double the gap of other structures (detailed results are shown in Table S4 in the ESM), indicating its higher chemical stability. The FPMD is also performed for the dimer of $W@Cu_{12}$, and results show that it is stable at 700 K (see Fig. S3 in the ESM). Combining the above analyses of binding energy, BCPs and IGMH, it has been learned that the interaction between superatoms is not enough to destroy the structure of single superatoms.

To further reveal the direct bonding mechanism of CM superatoms, the experimentally synthesized $W@Au_{12}$ was chosen as a model system for detailed analyses. The electronic configuration of $W@Au_{12}$ is $1S^21P^61D^{10}$ and the superatomic molecular orbitals (SAMOs) are listed in Fig. 2(a). Based on the $W@Au_{12}$ monomer, the direct bonding structure $W@Au_{12}$-$W@Au_{12}$ is shown in Fig. 2(b). There are eight chemical bonds between two monomers, and corresponding atoms are directly

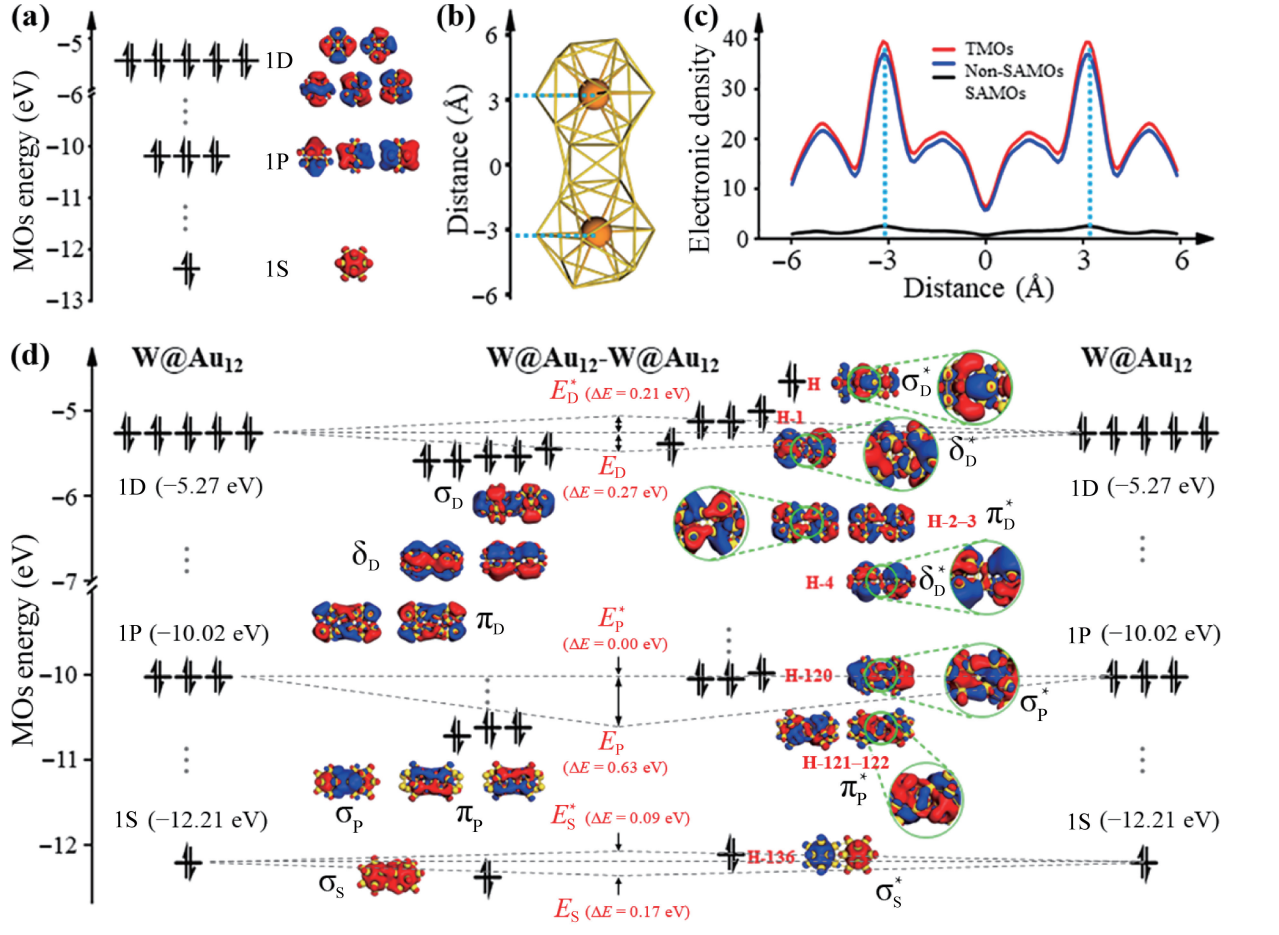

Figure 2 Orbital analysis of $W@Au_{12}$ and $W@Au_{12}$-$W@Au_{12}$. (a) The energy levels and SAMOs diagram of $W@Au_{12}$. (b) The structure of $W@Au_{12}$-$W@Au_{12}$. (c) The electron density of TMOs, SMOs, and non-SMOs of $W@Au_{12}$-$W@Au_{12}$. The light blue dotted line in (b) and (c) represents the position of the two central W atoms. (d) The energy levels of $W@Au_{12}$ and $W@Au_{12}$-$W@Au_{12}$, as well as the diagram of the bonding SMOs (σ_S, σ_P, π_P, π_D, δ_D, and σ_D) and the anti-bonding SMOs (σ_S^*, π_P^*, σ_P^* δ_D^*, π_D^*, and σ_D^*) of $W@Au_{12}$-$W@Au_{12}$. The value in brackets represents the energy difference between the average energy of SMOs and the average energy of SAMOs. Part of the middle part of the anti-bonding SMOs is magnified. HOMO is marked as H.

bonded (for details, see Fig. S4 in the ESM). In order to explore the bonding mechanism of the superatoms with closed shells, we first performed the electron density analysis on the orbitals of $W@Au_{12}$-$W@Au_{12}$ (Fig. 2(c)). The orbitals can be divided into three categories: total molecular orbitals (TMOs), SMOs, and non-SMOs. It is found that at the junction, the electron density value of non-SMOs is much higher than that of SMOs and close to TMOs. This proves that non-SMOs play a major effect on the combination of single superatoms.

Furthermore, the energy levels of $W@Au_{12}$ and $W@Au_{12}$-$W@Au_{12}$ are shown in Fig. 2(d) to clarify the contribution of SMOs in bonding. According to the concept of the super valence bond as well as the $1S^21P^61D^{10}$ electronic configuration of $W@Au_{12}$ [62, 63], it can be found that after the interaction of 1S SAMOs of two monomers, a bonding orbital σ_S and an anti-bonding orbital σ_S^* are formed; after the interaction of six 1P SAMOs of two monomers, one σ_P and two π_P bonding orbitals, and two π_P^* and one σ_P^* anti-bonding orbitals are formed; after the interaction of ten 1D SAMOs of two monomers, two π_D, two δ_D, and one σ_D bonding orbitals, and two π_D^*, two δ_D^*, and one σ_D^* anti-bonding orbitals are formed, respectively. So, the number of bonding and anti-bonding SMOs is 1:1 for $W@Au_{12}$-$W@Au_{12}$, and its electronic configuration is $1\sigma_S^2 1\sigma_S^{*2} 1\sigma_P^2 1\pi_P^4 1\pi_P^{*4} 1\sigma_P^{*2} 1\pi_D^4 1\delta_D^4 1\sigma_D^2 1\pi_D^{*4} 1\delta_D^{*4} 1\sigma_D^{*2}$. Among them, the bonding SMOs fused by SAMOs contribute to bonding. The anti-bonding SMOs represent the SAMOs just delocalized on each monomer [62], due to wave functions with opposite amplitudes at the connection become smaller after superposition. It is accepted that the front orbitals greatly affect the chemical bonds between units. For $W@Au_{12}$-$W@Au_{12}$, the HOMO–HOMO-4 are all anti-bonding orbitals, which proves that the anti-bonding orbitals of supermolecules play an essential effect in maintaining the stability of the geometric and electronic structure of monomers.

It is known that when two atoms bond, the same number of bonding and anti-bonding orbitals are formed, and equal amounts of energy are absorbed and released. This results in the inability of noble gas atoms to form diatomic molecules in the natural environment. Compared with noble atoms, closed-shell coinage metal superatoms are composed of atoms with superatomic molecular orbitals exhibiting atomic orbital symmetry, but due to the high activity of coinage metals, anti-bonding SMOs can be partially fused. Therefore, the formation of anti-bonding SMO absorbs less energy than the bonding SMO releases, resulting in a lower energy system. By comparing the energy changes of the orbitals before and after bonding, the contribution of the bonding and anti-bonding orbitals to chemical bonding can be further revealed [64]. As shown in Fig. 2(d), the energy of the σ_S SMO is lower than that of S SAMO, and the energy of the σ_S^* SMO is greater than the energy of S SAMO. P and D SMOs are also confirming this rule. Therefore, SAMOs form an equal number of bonding and anti-bonding SMOs that release more energy than absorb, resulting in they can bond. And the total effects of bonding orbitals and anti-bonding orbitals contribute to bonding.

The contribution of atoms at junction for anti-bonding SMOs is listed in Table 1 (detailed contributions are shown in Fig. S4 in the ESM and Table S5 in the ESM). Orbital diagram shows that the σ_S^* SMO formed by two S SAMOs completely exhibits an anti-bonding effect. However, the atomic contribution at the junction is small, and the superposition of the positive and negative orbital wave functions reduces the electron density by a relatively small amount, resulting in a partial weakening of the nuclear repulsion between the superatoms. Thus, σ_S^* SMO has a weak anti-bonding effect and a slightly higher orbital energy than S SAMO. The π_P^* and σ_P^* SMOs are composed of double degenerated HOMO-121–122 SMOs and non-degenerated HOMO-120 SMO. These three SMOs show that while the monomeric SAMOs are still delocalized on the monomers, the connection is fused (see Fig. 2(d)). Higher atomic contribution of eight atoms at connection contributes to bond, leading lower-energy of anti-bonding SMOs. π_D^*, δ_D^*, and σ_D^* SMOs show more complex bonding effects. The orbitals of atoms at the junction fused and contributed to bonding for HOMO-4 and double degenerate HOMO-2–3, which reduced the orbital energy. HOMO-1 exhibits complete antibonding with 30% large atomic contribution at the junction, and the superposition of positive and negative orbital wavefunctions reduces the electron density relatively large, resulting in higher energy orbitals. For HOMO, it is partially fused at the connection, which in turn leads to more phase-opposite orbital arrangements, resulting in HOMO has higher orbital energy. Thus, although the anti-bonding SMOs follow the largest negative overlap, the atomic orbitals of the Au atoms belonging to the two monomers represent different effects depending on phase and atomic orbital contribution. Finally, the multi-effect anti-bonding SMOs are not only keeping the electronic structure of the monomers basically unchanged, but also forming a link through several atomic orbitals at the junction. This leads to a decrease in the energy of anti-bonding SMOs, which further results in the total energy of bonding and anti-bonding SMOs being lower than the SAMOs.

Table 1 The contribution of atoms at connection for anti-bonding SMOs

Anti-bonding SMOs	Orbitals labels	Contribution (%)
σ_D^*	H	33.28
δ_D^*	H-1	30.12
δ_D^*	H-2	22.08
π_D^*	H-3	22.08
π_D^*	H-4	22.22
σ_P^*	H-120	46.25
π_P^*	H-121	48.38
π_P^*	H-122	48.40
σ_S^*	H-136	19.34

Further, focusing on the bonding process of the dimer, according to the distance between the central atoms of the two monomers, five structures were selected from far to near to study the changes of systems' geometric and electronic structures. As shown in Fig. 3, they are marked as initial structure, middle structure 1 (M1), direct bonded structure, middle structure 2 (M2), and terminal structure, respectively. In these structures, the distances between the central atoms are 11.0, 9, 6.27, 5, and 4 Å, respectively. The energy curve shows that as the monomers approach, the energy of the system first decreases and then increases, and the energy of the direct bonded structure is the local minimum, indicating that its energy is smaller than the coalesced structure. This confirms that the closed-shell CM superatoms can be directly bonded without destroying the structure of monomers.

To visually analyze the charge behavior between superatoms, the charge density difference (CDD) analysis was used to study the charge transfer with the change of the distance between two monomers (in Fig. 3), and then to understand their bonding behavior. The results show that the charge transfer of the five structures is not the same: In the initial structure, because the two monomers are too far apart, there is no charge transfer; in M1, two monomers are about to bond, and the charges begin to concentrate at the junction; for the direct bonded structure, the overall exhibits more charge transfer, and more charges

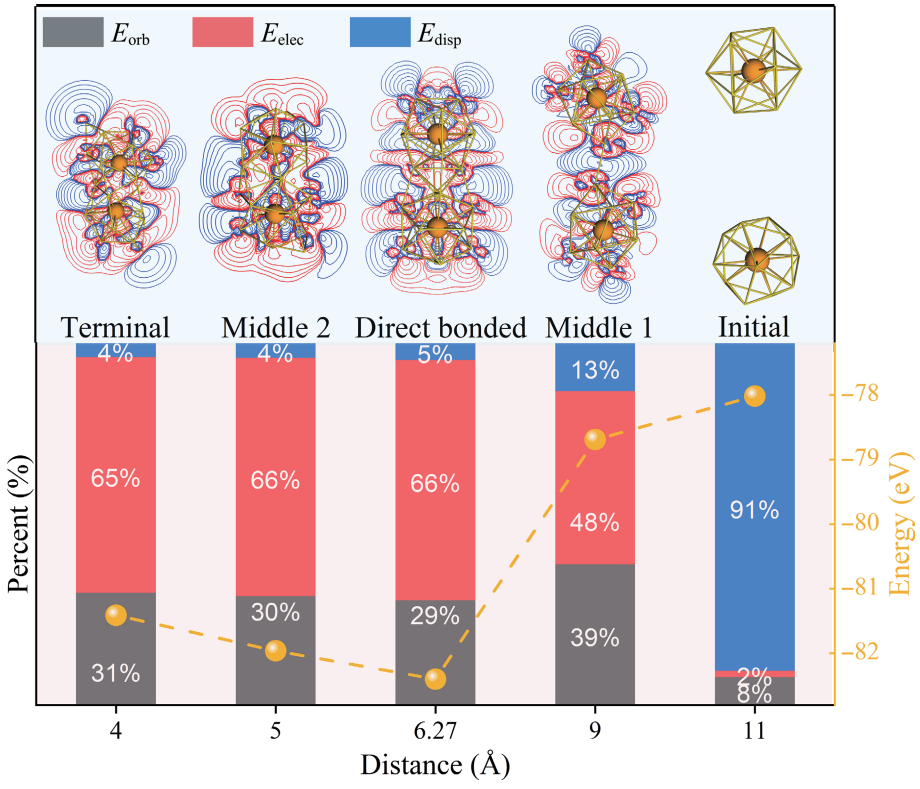

Figure 3 Analysis of energy, CDD, and EDA during superatomic bonding. Two monomers form five structures from far (right) to near (left), which are initial structure, M1, stable structure, M2, and termination structure. The horizontal axis represents the distance between two central W atoms. The yellow dashed line corresponds to the structural energy on the *y*-axis on the right. The blue and red around structures' diagrams indicate the accumulation and dissipation of electrons. The left axis corresponds to the percentage of each item in the energy decomposition analysis. E_{orb}, E_{elstat}, and E_{disp} represent orbital, electrostatic, and dispersion interactions, respectively.

accumulate at the junction. This behavior of charges gathering at the junction proves that two W@Au_{12} monomers can be bonded. For M2 and terminal structures, the charges are no longer mainly transferred to the junction, which also confirms that two monomers coalesce together.

EDA is an effective method to quantitatively analyze the interaction between units. In Fig. 3, the result shows that the attractiveness of the initial structure is weak, mainly from the long-range dispersion interaction. For the M1 structure, as the distance between the monomers decreases, electrostatic interaction begins to take up the main contribution. For the direct bonded structure, electrostatic interaction accounts for more than 66% of the total attractive force, and orbital interaction and dispersion interaction account for 29% and 5%. Therefore, electrostatic force plays a leading role in bonding. This weak interaction helps to achieve assembly while maintaining the structure of monomers. For M2 and the terminal structure, due to the coalescence of monomers, the orbital interaction increases. Although the two central W atoms approach during the coalescing process, the overall spatial position of the golden cage does not change significantly. Therefore, the composition of the interaction is similar to the stable structure.

The above analysis shows that W@Au_{12} has the potential as a self-assembly unit. Thus, the one-dimensional (1D) and two-dimensional (2D) structures are further assembled (Fig. 4). The results of geometric optimization show that the bond length of the monomers has just slightly changed after assembly (see Table S6 in the ESM), which can maintain its structural framework. In order to compare the electronic structure properties before and after assembly, the density of states analysis (DOS) analysis was performed on monomer, dimer, trimer-1D, trimer-2D, tetramer-1D, and tetramer-2D, as shown in Fig. 4. The overall trend of these DOS curves is the same, but the peak has a slight shift. This shows that the electronic structure of the assembled structure is similar to the monomer, which can also be inferred that they have similar chemical properties. Their HOMO-LUMO gaps are also listed, which can be used to measure chemical stability. The results show that the HOMO-LUMO gap of monomer, dimer, trimer-1D, trimer-2D, tetramer-1D, and tetramer-2D reach 1.75, 0.93, 0.82, 0.65, 0.74, and 0.74 eV, respectively, and the HOMO-LUMO gap decreases with the increase of the number of units, and finally tends to be flat. Among them, the trimer-2D has the smallest HOMO-LUMO gap due to the largest deformation. The change of HOMO-LUMO gap with the number of units helps to achieve different functional applications.

Evidently, materials with new properties can be designed using CM superatoms as building blocks. Although many assembly strategies, including ligand passivation, and sharing of atoms [65, 66], have been proposed to change material properties by regulating the type of ligands and the number of shared atoms, the delicate and precise tuning their atomic structures and properties based on the individual nanoclusters (CM superatoms) are impractical. In contrast, the mechanism of direct bottom-up assembly of closed-shell CM superatoms allows the design of material properties and functions while maintaining monomeric properties. Therefore, the controllable design of the nanomaterials with collective properties using the monomers as the Lego blocks and avoid the negative effects of introducing ligands is feasible.

4 Conclusions

In summary, we demonstrated that the sixth subgroup elements (including Cr, Mo, and W) embedded in CM (Cu, Ag, and Au) cages are closed-shell superatoms. The extremely high stability and the small interaction between superatoms guarantee the direct chemical bonding between theses CM superatoms without losing

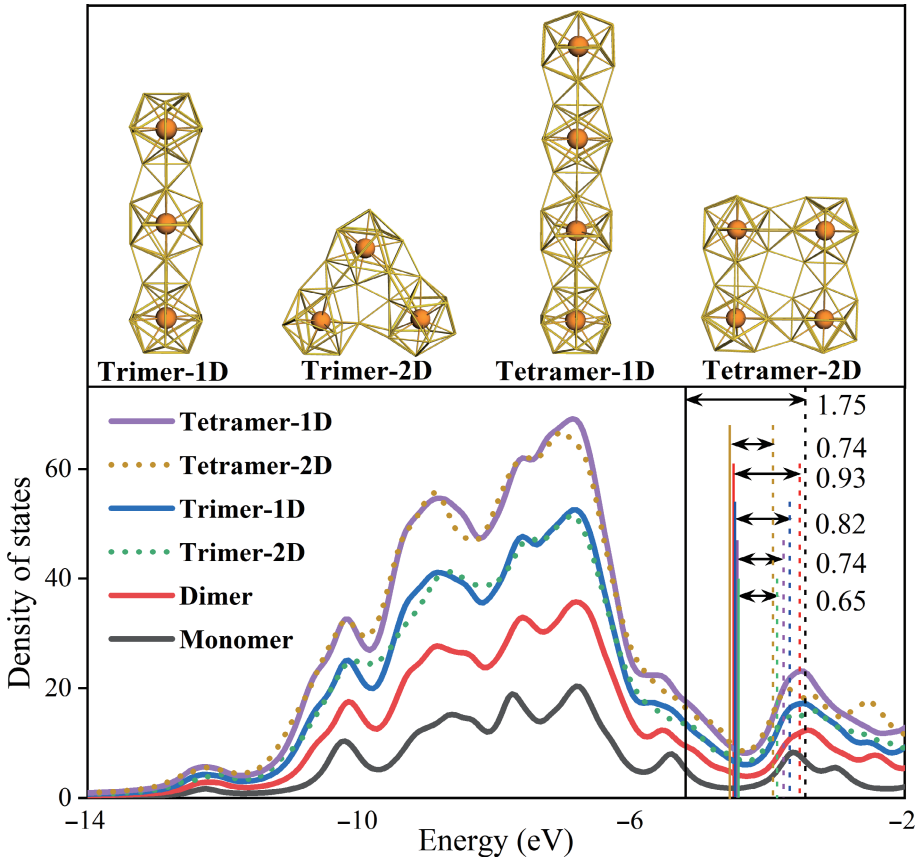

Figure 4 Assembled structures and their DOSs. 1D and 2D stand for one-dimension and two-dimension 1D. The vertical solid line and the dashed line represent HOMO and LUMO, respectively.

their original structures. The calculations show that the bonding nature can be attributed to the effect of an equal number of bonding SMOs and anti-bonding SMOs, which causes the interaction between superatoms to be weaker than the interaction within superatoms. For $W@Au_{12}$ superatom, a series of assembly structures were built based on the bottom-up strategy. Besides, the DOS analysis shows that the bonded structure has similar electronic structure properties to the monomer. These results can complement the assembly of CM clusters that are restricted by instability and ligands.

The direct bonding between the embedded CM superatoms has shown great application prospects in the assembly field, hoping to contribute to achieving collective properties and even revolutionary applications. Our research shows that the closed shell CM superatoms are promising units to construct different dimensional materials for different potential applications by changing its number. The new understanding of superatomic bonding established in this work is expected to realize non-coalesced assembly while maintaining their own properties, and provide a reference for future experimental design.

Acknowledgements

We would like to thank Ms. Zheng Liu and Ms. Aihua Cheng for the stimulating discussion. This work was supported by the National Science Foundation of China (Nos. 11974136 and 11674123). Z. G. W. also acknowledges the High-Performance Computing Center of Jilin University and National Supercomputing Center in Shanghai.

Electronic Supplementary Material: Supplementary material (further details for interaction analyses between two superatoms, structures and the change of bond length for homodimers, thermodynamic test of $W@Au_{12}$-$W@Au_{12}$ and $W@Cu_{12}$-$W@Cu_{12}$, stability analyses of W_2Au_{24} isomers, the contribution of atoms at junction for the anti-bonding SMOs as well as the bond length for $W@Au_{12}$ and its self-assembly structures.) is available in the online version of this article at https://doi.org/10.1007/s12274-022-4478-0.

References

[1] Doud, E. A.; Voevodin, A.; Hochuli, T. J.; Champsaur, A. M.; Nuckolls, C.; Roy, X. Superatoms in materials science. *Nat. Rev. Mater.* **2020**, *5*, 371–387.

[2] Li, J.; Li, X.; Zhai, H. J.; Wang, L. S. Au_{20}: A tetrahedral cluster. *Science* **2003**, *299*, 864–867.

[3] Desireddy, A.; Conn, B. E.; Guo, J. S.; Yoon, B.; Barnett, R. N.; Monahan, B. M.; Kirschbaum, K.; Griffith, W. P.; Whetten, R. L.; Landman, U. et al. Ultrastable silver nanoparticles. *Nature* **2013**, *501*, 399–402.

[4] Joshi, C. P.; Bootharaju, M. S.; Alhilaly, M. J.; Bakr, O. M. $[Ag_{25}(SR)_{18}]^-$:The "golden" silver nanoparticle. *J. Am. Chem. Soc.* **2015**, *137*, 11578–11581.

[5] Wang, Z. Y.; Wang, M. Q.; Li, Y. L.; Luo, P.; Jia, T. T.; Huang, R. W.; Zang, S. Q.; Mak, T. C. W. Atomically precise site-specific tailoring and directional assembly of superatomic silver nanoclusters. *J. Am. Chem. Soc.* **2018**, *140*, 1069–1076.

[6] Kwak, K.; Lee, D. Electrochemistry of atomically precise metal nanoclusters. *Acc. Chem. Res.* **2019**, *52*, 12–22.

[7] Xu, W. W.; Zhu, B. E.; Zeng, X. C.; Gao, Y. A grand unified model for liganded gold clusters. *Nat. Commun.* **2016**, *7*, 13574.

[8] Liu, X.; Xu, W. W.; Huang, X. Y.; Wang, E. D.; Cai, X.; Zhao, Y.; Li, J.; Xiao, M.; Zhang, C. F.; Gao, Y. et al. De novo design of $Au_{36}(SR)_{24}$ nanoclusters. *Nat. Commun.* **2020**, *11*, 3349.

[9] Lei, Z.; Wan, X. K.; Yuan, S. F.; Guan, Z. J.; Wang, Q. M. Alkynyl approach toward the protection of metal nanoclusters. *Acc. Chem. Res.* **2018**, *51*, 2465–2474.

[10] Jadzinsky, P. D.; Calero, G.; Ackerson, C. J.; Bushnell, D. A.;

Kornberg, R. D. Structure of a thiol monolayer-protected gold nanoparticle at 1. *1 Å resolution. Science* **2007**, *318*, 430–433.
[11] Klajn, R.; Bishop, K. J. M.; Fialkowski, M.; Paszewski, M.; Campbell, C. J.; Gray, T. P.; Grzybowski, B. A. Plastic and moldable metals by self-assembly of sticky nanoparticle aggregates. *Science* **2007**, *316*, 261–264.
[12] Wu, X.; Lu, X. Dimetalloendofullerene $U_2@C_{60}$ has a U−U multiple bond consisting of sixfold one-electron-two-center bonds. *J. Am. Chem. Soc.* **2007**, *129*, 2171–2177.
[13] Li, J.; Huang, H. C.; Chen, J.; Bu, Y. X.; Cheng, S. B. Organic ligand mediated evolution from aluminum-based superalkalis to superatomic molecules and one-dimensional nanowires. *Nano Res,* **2022**, *15*, 1162–1170.
[14] Guo, P.; Gao, Y. Coalescence of Au nanoparticles without ligand detachment. *Phys. Rev. Lett.* **2020**, *124*, 066101.
[15] Yin, B. Q.; Luo, Z. X. Coinage metal clusters: From superatom chemistry to genetic materials. *Coord. Chem. Rev.* **2021**, *429*, 213643.
[16] Williamson, M. J.; Tromp, R. M.; Vereecken, P. M.; Hull, R.; Ross, F. M. Dynamic microscopy of nanoscale cluster growth at the solid–liquid interface. *Nat. Mater.* **2003**, *2*, 532–536.
[17] Fiorio, J. L.; Barbosa, E. C. M.; Kikuchi, D. K.; Camargo, P. H. C.; Rudolph, M.; Hashmi, A. S. K.; Rossi, L. M. Piperazine-promoted gold-catalyzed hydrogenation: The influence of capping ligands. *Catal. Sci. Technol.* **2020**, *10*, 1996–2003.
[18] Ma, Y. Y.; Zhang, S.; Chang, C. R.; Huang, Z. Q.; Ho, J. C.; Qu, Y. Semi-solid and solid frustrated Lewis pair catalysts. *Chem. Soc. Rev.* **2018**, *47*, 5541–5553.
[19] Fiorio, J. L.; López, N.; Rossi, L. M. Gold-ligand-catalyzed selective hydrogenation of alkynes into cis-alkenes via H_2 heterolytic activation by frustrated Lewis pairs. *ACS Catal.* **2017**, *7*, 2973–2980.
[20] Izquierdo, F.; Manzini, S.; Nolan, S. P. The use of the sterically demanding IPr* and related ligands in catalysis. *Chem. Commun.* **2014**, *50*, 14926–14937.
[21] Chen, S. P.; Li, M. F.; Yu, S.; Louisia, S.; Chuang, W.; Gao, M. Y.; Chen, C. B.; Jin, J. B.; Salmeron, M. B.; Yang, P. D. Ligand removal of Au_{25} nanoclusters by thermal and electrochemical treatments for selective CO_2 electroreduction to CO. *J. Chem. Phys.* **2021**, *155*, 051101.
[22] Xie, W. Y.; Zhu, Y.; Wang, J. P.; Cheng, A. H.; Wang, Z. G. Magnetic coupling induced self-assembly at atomic level. *Chin. Phys. Lett.* **2019**, *36*, 116401.
[23] Iwasa, T.; Nakajima, A. Geometric, electronic, and optical properties of monomer and assembly of endohedral aluminum superatomic clusters. *J. Phys. Chem. C* **2013**, *117*, 21551–21557.
[24] Robles, R.; Khanna, S. N. Magnetism in assembled and supported silicon endohedral cages: First-principles electronic structure calculations. *Phys. Rev. B* **2009**, *80*, 115414.
[25] Singh, A.; Sen, P. Finding the right substrate support for magnetic superatom assembly from density functional calculations. *Phys. Rev. B* **2015**, *91*, 035438.
[26] Ohta, T.; Shibuta, M.; Tsunoyama, H.; Eguchi, T.; Nakajima, A. Charge transfer complexation of Ta-encapsulating $Ta@Si_{16}$ superatom with C_{60}. *J. Phys. Chem. C* **2016**, *120*, 15265–15271.
[27] Du, Q. Y.; Wang, Z.; Zhou, S.; Zhao, J. J.; Kumar, V. Searching for cluster Lego blocks for three-dimensional and two-dimensional assemblies. *Phys. Rev. Mater.* **2021**, *5*, 066001.
[28] Khanna, S. N.; Jena, P. Atomic clusters: Building blocks for a class of solids. *Phys. Rev. B* **1995**, *51*, 13705–13716.
[29] Bergeron, D. E. ; Castleman, A. W. Jr. ; Morisato, T. ; Khanna, S. N. Formation of $Al_{13}I^-$: Evidence for the superhalogen character of Al_{13}. *Science* **2004**, *304*, 84–87.
[30] Yoon, B.; Hakkinen, H.; Landman, U.; Worz, A. S.; Antonietti, J. M.; Abbet, S.; Judai, K.; Heiz, U. Charging effects on bonding and catalyzed oxidation of CO on Au_8 clusters on MgO. *Science* **2005**, *307*, 403–407.
[31] Reber, A. C.; Khanna, S. N.; Castleman, A. W. Superatom compounds, clusters, and assemblies: Ultra alkali motifs and architectures. *J. Am. Chem. Soc.* **2007**, *129*, 10189–10194.
[32] Luo, Z. X.; Castleman, A. W. Special and general superatoms. *Acc. Chem. Res.* **2014**, *47*, 2931–2940.
[33] Liu, G. X.; Pinkard, A.; Ciborowski, S. M.; Chauhan, V.; Zhu, Z. G.; Aydt, A. P.; Khanna, S. N.; Roy, X.; Bowen, K. H. Tuning the electronic properties of hexanuclear cobalt sulfide superatoms via ligand substitution. *Chem. Sci.* **2019**, *10*, 1760–1766.
[34] Lee, J.; Yang, J.; Kwon, S. G.; Hyeon, T. Nonclassical nucleation and growth of inorganic nanoparticles. *Nat. Rev. Mater.* **2016**, *1*, 16034.
[35] Zhou, T. W.; Wang, M.; Zang, Z. G.; Tang, X. S.; Fang, L. Two-dimensional lead-free hybrid halide perovskite using superatom anions with tunable electronic properties. *Sol. Energy Mater. Sol. Cells* **2019**, *191*, 33–38.
[36] Gao, Y.; Wang, B.; Lei, Y. Y.; Teo, B. K.; Wang, Z. G. Actinide-embedded gold superatom models: Electronic structure, spectroscopic properties, and applications in surface-enhanced Raman scattering. *Nano Res.* **2016**, *9*, 622–632.
[37] Shen, H.; Xiang, S. J.; Xu, Z.; Liu, C.; Li, X. H.; Sun, C. F.; Lin, S. C.; Teo, B. K.; Zheng, N. F. Superatomic Au_{13} clusters ligated by different N-heterocyclic carbenes and their ligand-dependent catalysis, photoluminescence, and proton sensitivity. *Nano Res.* **2020**, *13*, 1908–1911.
[38] Liu, J.; Guo, P.; Zheng, J. M.; Zhao, P. J.; Jiang, Z. Y.; Shen, L. Self-assembly of a two-dimensional sheet with $Ta@Si_{16}$ superatoms and its magnetic and photocatalytic properties. *J. Phys. Chem. C* **2020**, *124*, 6861–6870.
[39] Liu, L. R.; Cheng, L. J.; Yang, J. L. The superatomic molecule theory of metal clusters. *Sci. Sin. :Chim.* **2018**, *48*, 143–153.
[40] Mingos, D. M. P. Bonding in molecular clusters and their relationship to bulk metals. *Chem. Soc. Rev.* **1986**, *15*, 31–61.
[41] Rodriguez, J. A.; Goodman, D. W. The nature of the metal-metal bond in bimetallic surfaces. *Science* **1992**, *257*, 897–903.
[42] Perdew, J. P. Density-functional approximation for the correlation energy of the inhomogeneous electron gas. *Phys. Rev. B* **1986**, *33*, 8822–8824.
[43] Becke, A. D. Density-functional exchange-energy approximation with correct asymptotic behavior. *Phys. Rev. A* **1988**, *38*, 3098–3100.
[44] Van Lenthe, E.; Ehlers, A.; Baerends, E. J. Geometry optimizations in the zero order regular approximation for relativistic effects. *J. Chem. Phys.* **1999**, *110*, 8943–8953.
[45] Morokuma, K. Molecular orbital studies of hydrogen bonds. *III. C=O···H–O hydrogen bond in $H_2CO···H_2O$ and $H_2CO···2H_2O$. J. Chem. Phys.* **1971**, *55*, 1236–1244.
[46] Ziegler, T.; Rauk, A. On the calculation of bonding energies by the Hartree Fock Slater method: I. *The transition state method. Theor. Chim. Acta* **1977**, *46*, 1–10.
[47] Te Velde, G.; Bickelhaupt, F. M.; Baerends, E. J.; Guerra, C. F.; Van Gisbergen, S. J. A.; Snijders, J. G.; Ziegler, T. Chemistry with ADF. *J. Comput. Chem.* **2001**, *22*, 931–967.
[48] Frisch, M. J.; Trucks, G. W.; Schlegel, H. B.; Scuseria, G. E.; Robb, M. A.; Cheeseman, J. R.; Scalmani, G.; Barone, V.; Mennucci, B.; Petersson, G. A. et al. *Gaussian 09*; Gaussian, Inc.: Wallingford, CT, USA, 2013.
[49] Lu, T.; Chen, F. W. Multiwfn: A multifunctional wavefunction analyzer. *J. Comput. Chem.* **2012**, *33*, 580–592.
[50] Car, R.; Parrinello, M. Unified approach for molecular dynamics and density-functional theory. *Phys. Rev. Lett.* **1985**, *55*, 2471–2474.
[51] Hutter, J.; Iannuzzi, M.; Schiffmann, F.; VandeVondele, J. CP2K:Atomistic simulations of condensed matter systems. WIREs Comput. Mol. *Sci.* **2014**, *4*, 15–25.
[52] Pham, H. T.; Cuong, N. T.; Tam, N. M.; Tung, N. T. A systematic investigation on $CrCu_n$ clusters with n = 9–16: Noble gas and tunable magnetic property. *J. Phys. Chem. A* **2016**, *120*, 7335–7343.
[53] Chen, L.; Wang, Z. G.; Li, Z. Q.; Zhang, R. Q. Chemical coupling SERS properties of pyridine on silver-caged metal clusters $M@Ag_{12}$ ($M = V^-, Nb^-, Ta^-$, Cr, Mo, W, Mn^+, Tc^+, Re^+). *J. Electron. Mater.* **2017**, *46*, 3904–3909.
[54] Nijamudheen, A.; Jose, D.; Datta, A. Metal encapsulation mediated planar to three dimensional structural transformation in Au-clusters: The venus flytrap effect. *Comput. Theor. Chem.* **2011**, *966*, 133–136.
[55] Li, X.; Kiran, B.; Li, J.; Zhai, H. J.; Wang, L. S. Experimental observation and confirmation of icosahedral $W@Au_{12}$ and $Mo@Au_{12}$ molecules. *Angew. Chem. , Int. Ed.* **2002**, *41*, 4786–4789.

[56] Pyykkö, P.; Runeberg, N. Icosahedral WAu_{12}: A predicted closed-shell species, stabilized by aurophilic attraction and relativity and in accord with the 18-electron rule. *Angew. Chem. , Int. Ed.* **2002**, *41*, 2174–2176.
[57] Pyykkö, P. Understanding the eighteen-electron rule. *J. Organomet. Chem.* **2006**, *691*, 4336–4340.
[58] Park, S.; Kim, G.; Kwon, Y. K. First-principles investigation on dimerization of metal-encapsulated gold nanoclusters. *RSC Adv.* **2014**, *4*, 192–198.
[59] Bader, R. F. W. Atoms in molecules. *Acc. Chem. Res.* **1985**, *18*, 9–15.
[60] Bianchi, R.; Gervasio, G.; Marabello, D. Experimental electron density analysis of $Mn_2(CO)_{10}$: Metal–metal and metal–ligand bond characterization. *Inorg. Chem.* **2000**, *39*, 2360–2366.
[61] Lu, T.; Chen, Q. X. Independent gradient model based on Hirshfeld partition: A new method for visual study of interactions in chemical systems. *J. Comput. Chem.* **2022**, *43*, 539–555.
[62] Cheng, L. J.; Yang, J. L. Communication: New insight into electronic shells of metal clusters: Analogues of simple molecules. *J. Chem. Phys.* **2013**, *138*, 141101.
[63] Cheng, L. J.; Zhang, X. Z.; Jin, B. K.; Yang, J. L. Superatom-atom super-bonding in metallic clusters: A new look to the mystery of an Au_{20} pyramid. *Nanoscale* **2014**, *6*, 12440–12444.
[64] Wan, Q. Y.; Yang, J.; To, W. P.; Che, C. M. Strong metal–metal Pauli repulsion leads to repulsive metallophilicity in closed-shell d^8 and d^{10} organometallic complexes. *Proc. Natl. Acad. Sci. USA* **2021**, *118*, e2019265118.
[65] Luo, Z. X.; Reber, A. C.; Jia, M. Y.; Blades, W. H.; Khanna, S. N.; Castleman, A. W. Jr. *What determines if a ligand activates or passivates a superatom cluster? Chem. Sci.* **2016**, *7*, 3067–3074.
[66] Cheng, L. J.; Ren, C. D.; Zhang, X. Z.; Yang, J. L. New insight into the electronic shell of $Au_{38}(SR)_{24}$: A superatomic molecule. *Nanoscale* **2013**, *5*, 1475–1478.